nature communications

Article

https://doi.org/10.1038/s41467-023-40373-z

# Giant room-temperature nonlinearities in a monolayer Janus topological semiconductor

Received: 19 March 2023

Accepted: 24 July 2023

Published online: 16 August 2023

Check for updates

Jiaojian Shi[1,2,13], Haowei Xu[3,13], Christian Heide[4,5], Changan HuangFu[6], Chenyi Xia[1,2], Felipe de Quesada[1,2], Hongzhi Shen[7], Tianyi Zhang[8], Leo Yu[9], Amalya Johnson[1], Fang Liu[5,10], Enzheng Shi[7], Liying Jiao[6], Tony Heinz[5,9], Shambhu Ghimire[5], Ju Li[3,11], Jing Kong[8], Yunfan Guo[12] ✉ & Aaron M. Lindenberg[1,2,5] ✉

Nonlinear optical materials possess wide applications, ranging from terahertz and mid-infrared detection to energy harvesting. Recently, the correlations between nonlinear optical responses and certain topological properties, such as the Berry curvature and the quantum metric tensor, have attracted considerable interest. Here, we report giant room-temperature nonlinearities in non-centrosymmetric two-dimensional topological materials—the Janus transition metal dichalcogenides in the 1 *T'* phase, synthesized by an advanced atomic-layer substitution method. High harmonic generation, terahertz emission spectroscopy, and second harmonic generation measurements consistently show orders-of-the-magnitude enhancement in terahertz-frequency nonlinearities in 1 *T'* MoSSe (e.g., > 50 times higher than 2*H* $MoS_2$ for 18$^{th}$ order harmonic generation; > 20 times higher than 2*H* $MoS_2$ for terahertz emission). We link this giant nonlinear optical response to topological band mixing and strong inversion symmetry breaking due to the Janus structure. Our work defines general protocols for designing materials with large nonlinearities and heralds the applications of topological materials in optoelectronics down to the monolayer limit.

Advances in nonlinear optics empower a plethora of applications, such as attosecond light sources based on high harmonic generation (HHG) and photodetectors for sensitive terahertz (THz) detection at elevated temperatures[1–4]. Inherently, the nonlinear optical properties of materials are connected with their magnetic structures[5,6], crystalline symmetries[7,8], and electronic band topologies. In particular, nontrivial band topologies lead to exotic electronic dynamics and enhanced optical responses[9–14]. Notable examples include anomalous HHG in various classes of topological materials[15–18]. The observation of enhanced optical responses in topological materials

[1]Department of Materials Science and Engineering, Stanford University, Stanford, CA 94305, USA. [2]Stanford Institute for Materials and Energy Sciences, SLAC National Accelerator Laboratory, Menlo Park, CA 94025, USA. [3]Department of Nuclear Science and Engineering, Massachusetts Institute of Technology, Cambridge, MA 02139, USA. [4]Department of Applied Physics, Stanford University, Stanford, CA 94305, USA. [5]Stanford PULSE Institute, SLAC National Accelerator Laboratory, Menlo Park, CA 94025, USA. [6]Key Laboratory of Organic Optoelectronics and Molecular Engineering of the Ministry of Education, Department of Chemistry, Tsinghua University, 100084 Beijing, China. [7]School of Engineering, Westlake University, 310024 Hangzhou, China. [8]Department of Electrical Engineering and Computer Science, Massachusetts Institute of Technology, Cambridge, MA 02139, USA. [9]E. L. Ginzton Laboratory, Stanford University, Stanford, CA 94305, USA. [10]Department of Chemistry, Stanford University, Stanford, CA 94305, USA. [11]Department of Materials Science and Engineering, Massachusetts Institute of Technology, Cambridge, MA 02139, USA. [12]Key Laboratory of Excited-State Materials of Zhejiang Province, Department of Chemistry, State Key Laboratory of Silicon and Advanced Semiconductor Materials, Zhejiang University, 310058 Hangzhou, China. [13]These authors contributed equally: Jiaojian Shi, Haowei Xu. ✉e-mail: yunfanguo@zju.edu.cn; aaronl@stanford.edu

have been found primarily in three-dimensional systems until now[12,13,15–17,19]. Designing two-dimensional (2D) platforms with strong optical responses is advantageous for optoelectronic applications at the nanoscale with easy controllability and scalability, but so far is limited to topologically trivial materials such as graphene[20] and 2*H*-phase transition metal dichalcogenides (TMDs)[21]. A promising topologically nontrivial candidate are the monolayer Janus TMDs (JTMDs) in the distorted octahedral (1 *T*′) phase[3]. Similar to 1 *T*′ pristine TMDs[22–24], 1 *T*′ JTMDs are topologically nontrivial with an inverted bandgap in the THz regime (tens of meV). Generally, a topologically protected band structure and small electronic bandgap result in larger Berry connections, larger electronic interband transition rate, and thus stronger optical response. In addition, by replacing the top layer chalcogen atoms (e.g., sulfur) in the monolayer 1 *T*′ TMDs with a different type of chalcogen (e.g., selenium), the resulting Janus structure has strong inversion asymmetry and electric polarization[25,26], which can further improve the nonlinear optical response.

In this work, we report experimental observations of giant nonlinearities at THz frequencies in monolayer 1 *T*′ JTMDs, which are synthesized via a room-temperature atomic-layer substitution (RT-ALS) method[27] under ambient conditions. It is revealed that, although the electromagnetic interaction occurs only in a single monolayer flake of 1 *T*′ MoSSe (~10–20 μm in transverse size), the generation of mid-infrared high harmonics, THz emission, and infrared second harmonic generation are all exceptionally efficient. Further comparison with topologically trivial TMDs and theoretical analyses indicate that the keys to such giant THz-frequency nonlinearities are strong inversion symmetry breaking and topological band mixing. Our results suggest that 1 *T*′ JTMDs is a promising material class that could lead to an era in THz/infrared sensing using atomically-thin materials. Our results also deepen the understanding of the fundamental mechanisms underlying strong nonlinear optical responses, which could have a profound influence in, for example, room-temperature THz detection and clean energy harvesting via the bulk photovoltaic effect[2,28].

## Results

### Multimodal nonlinearity characterization of 1 *T*′ MoSSe

The schematic illustration of multimodal characterization methods is shown in Fig. 1a. Our experiments investigated the THz-frequency nonlinearities of monolayer 1 *T*′ MoSSe with three different techniques, i.e., high harmonic generation (HHG)[29,30], THz emission spectroscopy (TES), and second harmonic generation (SHG). These techniques access nonlinear coefficients with different orders (2nd to 18th order) and spectral ranges (THz to infrared). As a comparison, we also studied the responses of monolayer 2*H* MoSSe, 1 *T*′ $MoS_2$, and 2*H* $MoS_2$ under the same measurement conditions. Such combined information unequivocally indicates giant THz-frequency nonlinearities for 1 *T*′ MoSSe. As shown in Fig. 1b, c, 1 *T*′ MoSSe and $MoS_2$ have distorted octahedral structures, with band inversion between metal *d*-orbitals and chalcogen *p*-orbitals[22]. In contrast, the *2H* phase is characterized by a trigonal prismatic structure and is topologically trivial. In this work, Janus 1 *T*′ MoSSe and *2H* MoSSe (Fig. 1d) are respectively converted from 1 *T*′ $MoS_2$ and *2H* $MoS_2$ by the room-temperature atomic-layer substitution method[2]. Highly reactive hydrogen radicals produced by a remote plasma were used to strip the top-layer sulfur atoms. Meanwhile, selenium vapor was supplied in the same low-pressure system to replace the missing sulfur, resulting in the asymmetric Janus MoSSe in 1 *T*′ phase and 2*H* phase. To confirm the fidelity of material conversion, Raman scattering measurements were performed due to their sensitivity to the crystal lattice structure (Fig. 1e). For Janus *2H* MoSSe, the positions of the $A_{1g}$ mode (~288 $cm^{-1}$) and $E_{2g}$ mode (~355 $cm^{-1}$) are consistent with literature results[2]; Meanwhile, the multiple *A*′ modes of Janus 1 *T*′ MoSSe located at ~226.2 $cm^{-1}$, ~298.4 $cm^{-1}$, ~429.8 $cm^{-1}$ agree well with the theoretical calculations as well, indicating the successful material substitution.

### Efficient high-harmonic generation

We first show highly efficient HHG from a single monolayer flake of 1 *T*′ MoSSe. The excitation source for HHG is mid-infrared (MIR) pulses with in-plane linear polarization at 5-μm wavelength, 1-kHz repetition rate, and ~ 20 MV/cm peak field strength (setup schematic shown in Supplementary Fig. 1). The HHG image acquired in 1 *T*′ MoSSe (Fig. 2a)

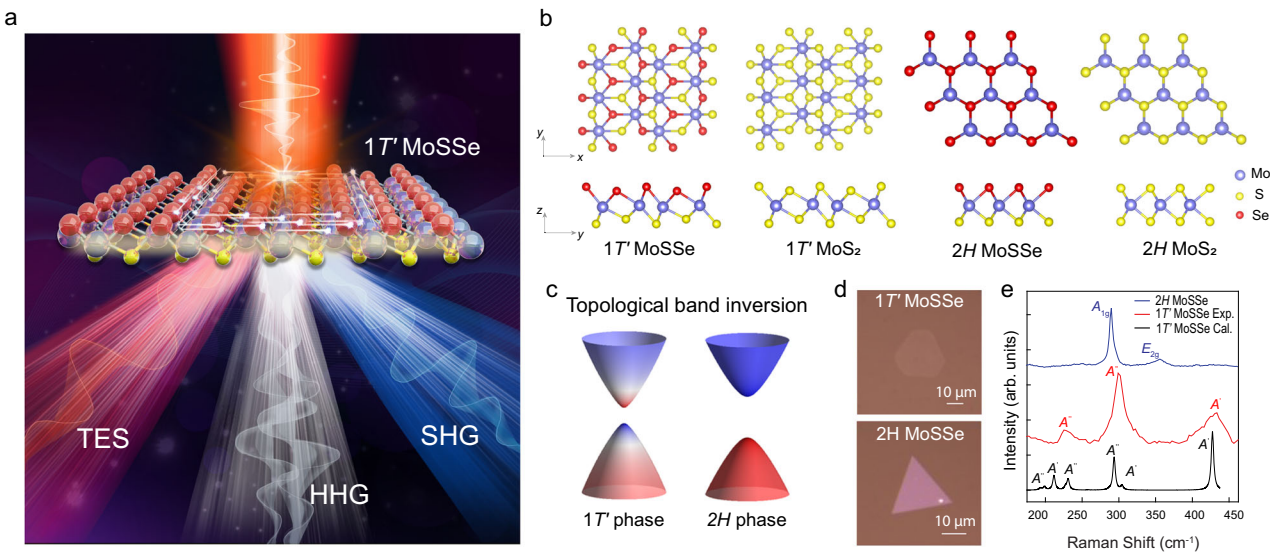


**Fig. 1 | Giant THz-frequency nonlinearities in 1 *T*′ MoSSe. a** Schematic illustration of THz emission spectroscopy (TES), mid-infrared high-harmonic generation (HHG), and near-infrared second harmonic generation (SHG) in 1 *T*′ MoSSe. **b** The lattice structure of 1 *T*′ MoSSe, 1 *T*′ $MoS_2$, 2*H* MoSSe, 2*H* $MoS_2$. **c** Schematic illustration of the topological band inversion in the 1 *T*′ phase (left) compared with the topologically trivial band structure of the 2*H* phase. The colormap (red and blue) indicates the wavefunction contributions from contributed by different atomic electron orbitals (e.g., chalcogen *p* and metal *d* orbitals.), and the 1 *T*′ phase exhibits a hybridization between the original valence and the conduction bands. **d** Optical images of 1 *T*′ MoSSe (top) and 2*H* MoSSe (bottom). **e** Experimental and theoretical Raman spectrum of 1 *T*′ MoSSe and experimental Raman spectrum of 2*H* MoSSe.

contains at least up to 18th order response, limited by our detection scheme. The even-order HHG, which is absent in bulk TMDs[30], is a direct consequence of the broken spatial symmetry of the monolayer Janus systems. We varied the incident MIR polarization and observed nearly perfect cancellation of HHG intensity at specific angles to one of the crystallographic axes, indicating the HHG signal originates from a single flake instead of an average over many flakes with random orientations (shown in Supplementary Fig. 4). This is consistent with the laser spot size ($1/e^2$ size) ~100 μm and the sparse flake-flake spacing (shown in Supplementary Fig. 4). The HHG intensity of single flake 1 *T′* MoSSe are further compared with that of millimeter-scale 2*H* $MoS_2$ under the same condition. Despite the irradiated flake being generally ~10 times smaller than the laser spot, the HHG of 1 *T′* MoSSe is over an order of magnitude stronger than that of the millimeter-scale *2H* $MoS_2$ with 100% coverage (Fig. 2b–d)[31]. The strong THz nonlinearity of 1 *T′* MoSSe is further confirmed by comparing it with other reference samples (2*H* MoSSe and 1 *T′* $MoS_2$). Figure 2e shows the HHG spectrum of 2*H* MoSSe, which has much weaker even-order harmonics than those of 1 *T′* MoSSe. Meanwhile, the HHG of 1 *T′* $MoS_2$, which is also topological nontrivial[22], shows relatively strong odd-order harmonics but no even-order harmonics, due to the inversion symmetry (Fig. 2f). Further semi-quantitative HHG efficiency comparison with other literature[16,30] is summarized in Table 1 showing clear advantages of 1 *T′* MoSSe over most solid-state bulk or film samples.

## Enhanced terahertz emission and second-harmonic generation

Dramatic enhancements in the TES and SHG measurements further validate giant nonlinearities in 1 *T′* MoSSe. Figure 3a shows the TES measurements under 800-nm laser excitation (details in Supplementary Fig. 2) on four kinds of chemical vapor deposition (CVD) grown samples (1 *T′* MoSSe, 1 *T′* $MoS_2$, *2H* MoSSe, and *2H* $MoS_2$), among which 1 *T′* MoSSe shows distinctly higher THz emission efficiency. We do not observe a detectable signal in 1 *T′* $MoS_2$ with the same excitation

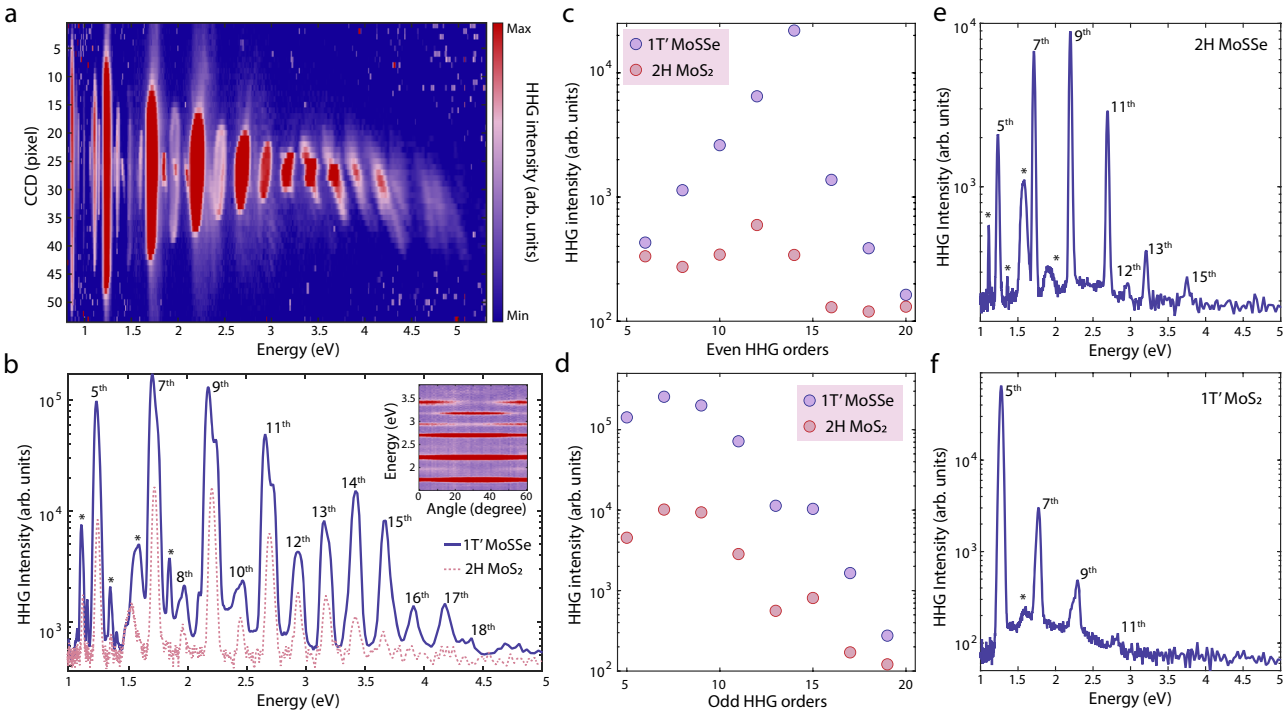


**Fig. 2 | Efficient mid-infrared high harmonic generation (HHG) in 1 *T′* MoSSe.** **a** HHG images of 1 *T′* MoSSe observed by CCD camera. HHG extends up to ~ 5 eV and is limited mainly by the cutoff of detection optics (e.g., aluminum mirrors and grating). **b** HHG spectrum of 1 *T′* MoSSe shown as the blue curve is over an order of magnitude stronger than the HHG from macroscopic monolayer 2*H* $MoS_2$ shown as the red dashed line. The inset shows 1 *T′* MoSSe HHG intensity as a function of MIR incident polarization angles. The cancellation of a few orders at some polarization angles indicates the signal is generated from a single flake. **c**, **d** Quantitative comparison of HHG intensity between 1 *T′* MoSSe and 2*H* $MoS_2$. Although the coverage of the 1 *T′* MoSSe sample is ~10 times lower than wafer-scale 2*H* $MoS_2$, the HHG signal is enhanced by over an order of magnitude, and orders as high as 18 or more are observed in 1 *T′* MoSSe while only up to 15th order can be observed in macroscopic monolayer 2*H* $MoS_2$. **e** The HHG spectrum of 2*H* MoSSe taken under the same conditions. The asterisks are artifacts due to high-order spectrometer diffraction. **f** HHG spectrum of 1 *T′* $MoS_2$. Even orders of 2*H* MoSSe and 1 *T′* $MoS_2$ are weak and indetectable compared with 1 *T′* MoSSe. The asterisks are artifacts due to high-order spectrometer diffraction.

**Table 1 | High-harmonic generation efficiency comparison of different materials**

| Material | Phase | Thickness[(i)] (nm) | Pump field[(ii)] (V/Å) | Excitation λ (nm) | Bandgap (eV) | 17th order rate (unit)[(iii)] | 18th order rate (unit)[(iv)] | Reference |
|---|---|---|---|---|---|---|---|---|
| 1 *T′* MoSSe | Solid | ~1 | 0.2 | 5000 | ~0.01 | ~100 (1) | ~20 (0.2) | This work |
| $Bi_2Se_3$ | Solid | ~1–10 | 0.25 | 5000 | ~0.3 | <0.01 ($10^{-4}$) | <0.002 ($2*10^{-5}$) | Ref. 16 |
| $MoS_2$ | Solid | ~1 | 0.4 | 5000 | ~1.8 | <1 ($10^{-2}$) | <0.1 ($10^{-3}$) | Ref. 30 |

Note: (i) Effective thickness is estimated and adopted here. (ii) The selected field strength of the excitation field. (iii)–(iv) The HHG efficiency is estimated and presented by emitted photon numbers/effective thickness/pump field. The numbers in the () are normalized to the 17th order for 1 *T′* MoSSe. Note the linear normalization to the pump field underestimates the difference between 1 *T′* MoSSe and other samples since HHG is a nonlinear process and incident field strength in 1 *T′* MoSSe is relatively low.

https://doi.org/10.1038/s41467-023-40373-z

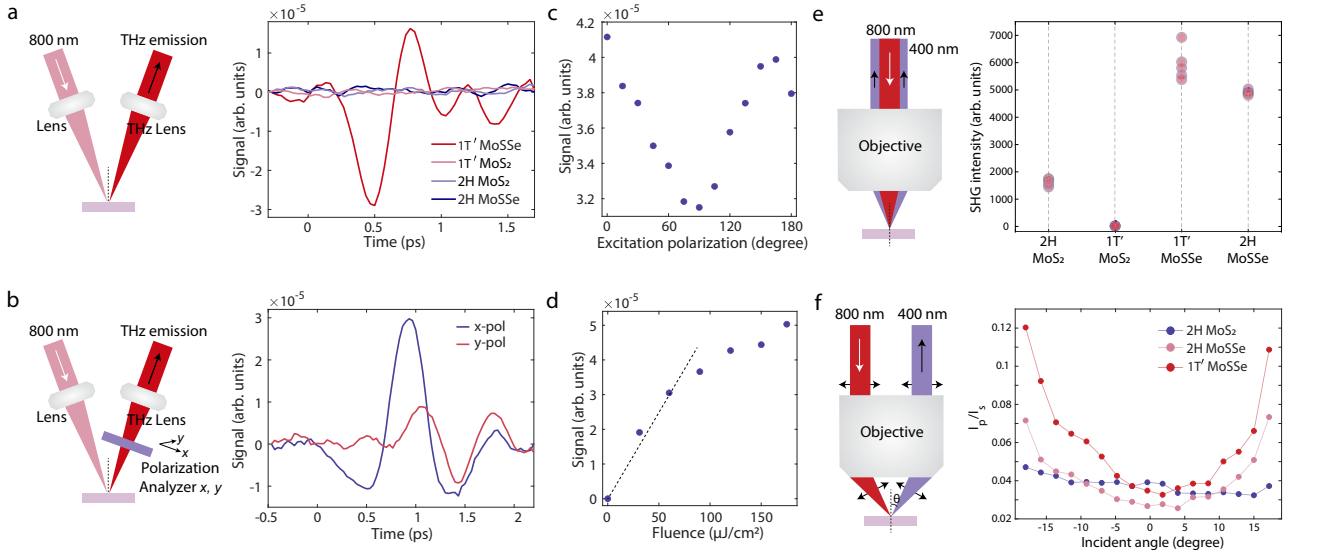


**Fig. 3 | THz emission spectroscopy and second harmonic generation of 1 *T′* MoSSe, 1 *T′* $MoS_2$, 2*H* MoSSe and 2*H* $MoS_2$.** **a** Left plot shows a schematic of THz emission setup. 1 *T′* MoSSe shows a dramatically enhanced THz emission signal compared with three other types of monolayer TMDs (right plot). **b** Left plot shows a schematic of polarization analysis of THz emission, which shows the emission contains a major in-plane component with a possible out-of-plane contribution (right plot). **c** Dependence of peak THz field on excitation polarization. No polarizers were used for the emitted THz signal. **d** Scaling of THz emission shows a linear dependence to incident power at low fluences and saturation at higher fluences. **e** Left plot shows a schematic of second harmonic generation with normally incident 800-nm excitation. The white arrow marks the incident 800-nm beam and the black arrow marks the SHG light. The right plot shows SHG intensity of five different flakes in each sample and shows SHG is enhanced in 1 *T′* MoSSe and 2*H* MoSSe compared with 1 *T′* $MoS_2$ and 2*H* $MoS_2$. **f** The left plot shows the schematic of the angle-resolved SHG setup that measures out-of-plane dipole. The white arrow marks the incident 800-nm beam and the black arrow marks the SHG light. The beam position at the objective back aperture is scanned perpendicular to the incident beam direction with a motorized stage, which tunes the incident angle $\theta$ accordingly. The right plot shows the angle-dependent SHG intensity ratio between *p* and *s* polarization ($I_p$ and $I_s$) in 1 *T′* MoSSe, 2*H* MoSSe, and 2*H* $MoS_2$. In the 1 *T′* MoSSe and 2*H* MoSSe, the $I_p/I_s$ ratio increases at non-normal incidence angles, indicative of out-of-plane dipoles. In 2*H* $MoS_2$, almost no change is observed as the incident angle varies.

fluence, consistent with its centrosymmetric structure, which forbids second-order nonlinear response. The weak TES signal in 2*H* $MoS_2$ has been attributed to an inefficient surface photocurrent[32,33]. The augmented TES in 1 *T′* MoSSe aligns with the theory that 1 *T′* TMDs exhibit giant nonlinearities at THz frequencies[3]. The polarization analysis of the THz emission (Fig. 3b) reveals the emitted radiation is mainly polarized in the lab-frame *x*-direction and contains a slightly weaker *y*-direction component (axis definition shown in Fig. 3b). Based on our experimental configuration, the *x*-direction emission has contributions from both in-plane and out-of-plane photoresponses, while the *y*-direction emission originates only from in-plane photoresponses. Thus, the observation of emission in the *y*-direction indicates the existence of an in-plane current contributing to the TES signal, but the stronger emission in the *x*-direction indicates there are likely significant contributions as well from out-of-plane currents. Further experiments are needed to disentangle the in-plane and out-of-plane contributions. For fixed excitation fluence, the peak THz field as a function of the pump polarization exhibits a sinusoidal modulation with a periodicity of approximately $\pi$ (Fig. 3c), reflecting the rank-two tensor nature of the photoresponses, which are second order in electric fields. Detailed analysis is included in Supplementary Figs. 5–10. Finally, the TES signal shows a linear dependence on the excitation fluence (Fig. 3d) at low fluences and continues to increase at higher fluences exceeding 60 μJ/cm², albeit with a smaller slope. Such phenomena are likely due to the combined effects of photocurrent saturation due to carrier generation[32] and nonlinearly increasing photocurrents (detailed discussion in Supplementary Note 5).

Figure 3e shows the SHG measurements on the four kinds of CVD-grown samples excited with 800-nm pulses (details in Supplementary Fig. 3). The SHG of several different flakes from each sample was measured to estimate the average intensity and flake-to-flake deviation. 2*H* $MoS_2$, 1 *T′* MoSSe, and 2*H* MoSSe show high SHG efficiency, and no SHG signal is detected in 1 *T′* $MoS_2$. In 1 *T′* MoSSe and 2*H* MoSSe, SHG is further enhanced by a factor of 4 and 3 compared to monolayer 2*H* $MoS_2$ respectively, for which high SHG efficiency has been extensively reported[21,34–36]. This highlights the importance of augmented inversion symmetry breaking in Janus structures, which improves even-order nonlinearities. The SHG efficiency in Janus-type samples is further amplified in an angle-resolved SHG measurement (Fig. 3f) that is particularly sensitive to out-of-plane dipoles[25]. In this experiment, the incident angle of the 800-nm fundamental beam deviates from the normal incidence so that the tilted incident beam provides a vertical electric field and interacts with the out-of-plane dipoles effectively. To exclude other geometric factors, an *s*-polarized SHG $I_s$ induced by an in-plane dipole with the same collection efficiency is measured and used to normalize *p*-polarized SHG $I_p$ that contains out-of-plane dipole contribution at non-normal incidence. For 1 *T′* MoSSe and 2*H* MoSSe, $I_p/I_s$ symmetrically increases as a function of the incident angle, while 2*H* $MoS_2$ shows much smaller angle-dependent changes. This confirms the presence of out-of-plane dipoles in Janus-type samples.

## Theoretical origin of giant terahertz-frequency nonlinearity

The experimental results above indicate that the optical nonlinearity of 1 *T′* MoSSe can be orders-of-magnitude (e.g., >50 times higher for 18th order HHG; >20 times higher for TES) stronger than those of 2*H* MoSSe. To understand this effect, we examine the microscopic mechanism underlying the strong THz-frequency nonlinear responses in 1 *T′* MoSSe. The band structures of 1 *T′* MoSSe is shown in Fig. 4a. The band inversion of 1 *T′* MoSSe happens around the $\Gamma$-point. Due to spin-orbit interaction, there is a band reopening at the $\pm\Lambda$-points (marked in Fig. 4a). When the Fermi level is inside the bandgap, the interband transition dipole (Berry connection) $r_{mn}(k) \equiv \langle mk|r|nk\rangle$ plays an essential role in optical processes[37], because it determines the strength of the dipole interaction between electrons and the electric fields. Here

https://doi.org/10.1038/s41467-023-40373-z

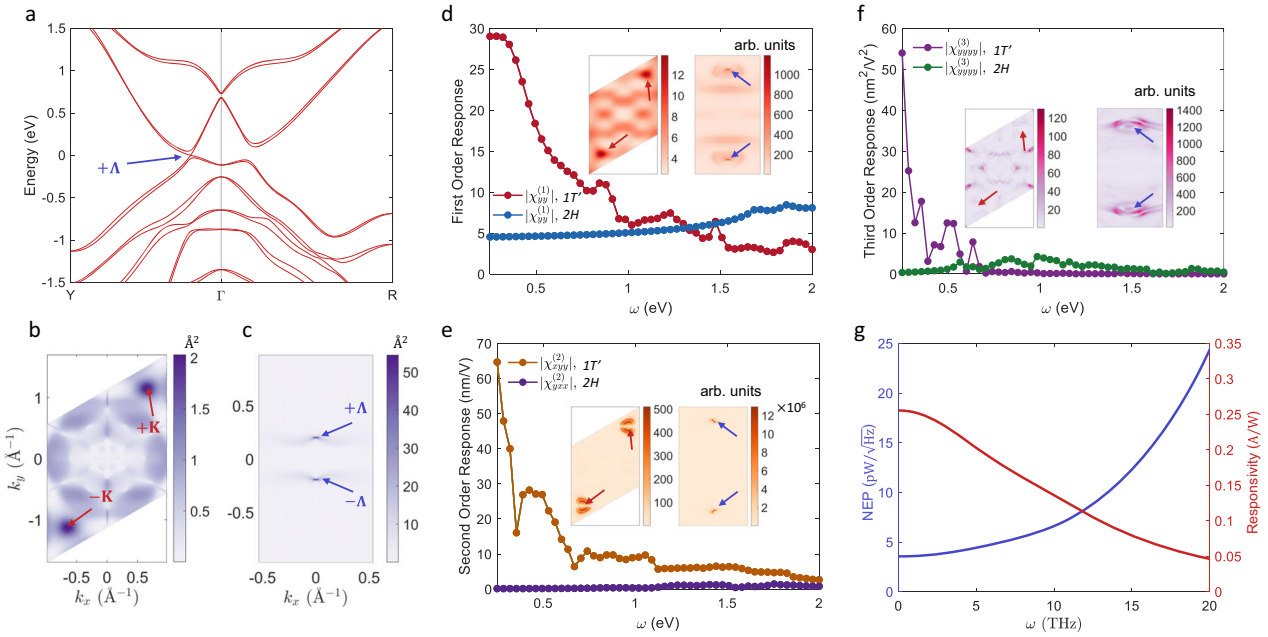


**Fig. 4 | Theoretical calculations of the nonlinear optical response of 2*H* and 1 *T*′ MoSSe. a** Band structure of 1 *T*′ MoSSe. The energy is offset to the valence band maximum. The band edge of 1 *T*′ MoSSe is located at the $\Lambda$ point, which is marked in (**a**). **b**, **c** The magnitude of the interband transition dipole $|r_{vc}(k)|$ for (**b**) 2*H* and (**c**) 1 *T*′ MoSSe in the first Brillouin zone. The colormap is in the unit of A. **d**–**f** First, second, and third-order optical responses of 1 *T*′ and 2*H* MoSSe as a function of incident light frequency ω. Insets of (**d**–**f**) show the *k*-resolved contributions (with arbitrary units) to the total response function at $\omega = 1$ eV for (left) 2*H* and (right) 1 *T*′ MoSSe. Red (blue) arrows in (**b**, **c**) and insets of (**d**–**f**) denote the $\pm K$ ($\pm\Lambda$) points, which are the bandedge of 2*H* (1 *T*′) MoSSe. In insets of (**d**–**f**), the Brillouin zone is zoomed in around the $\pm\Lambda$ points for 1 *T*′ MoSSe to give better visibility. **g** The NEP (left *y* axis) and photo-responsivity (right *y* axis) of 1 *T*′ JTMD THz detector as a function of the light frequency $\omega$.

*r* is the position operator, while $|mk\rangle$ is the electron wavefunction at band *m* and wavevector *k*. In Fig. 4b, c, we plot $|r_{vc}(k)|$ of 2*H* and 1 *T*′ MoSSe, where *v* (*c*) denotes the highest valence (lowest conduction) band. For 2*H* MoSSe, the maximum value of $|r_{vc}(k)|$ is around $\sim 2$ A near the band-edge ($\pm K$ points), while for 1 *T*′ MoSSe, $|r_{vc}(k)|$ can reach $\sim 50$ A near the band-edge ($\pm\Lambda$ points). Consequently, electrons in 1 *T*′ MoSSe would have stronger dipole interaction and hence faster interband transitions under light illumination. This is attributed to the topological enhancement, that is, band inversions in topological 1 *T*′ MoSSe lead to wavefunction hybridization and hence larger wavefunction overlap between valence and conduction bands near the band edge, which accelerates the interband transitions[3,38,39]. The calculated first, second, and third-order nonlinear susceptibilities of 2*H* and 1 *T*′ MoSSe are shown in Fig. 4d–f. For $\omega \lesssim 0.5$ eV, the responses of 1 *T*′ MoSSe are significantly stronger than those of 2*H* MoSSe. For $\omega \gtrsim 1$ eV, the responses of 1 *T*′ and 2*H* MoSSe are relatively close, consistent with experimental HHG, TES, and SHG measurements at different wavelengths. In the insets of Fig. 4d–f, we plot the *k*-resolved contributions $I^{(i)}(k)$ to the optical susceptibility at $\omega = 1$ eV (see "Methods" for details). Notably, the maximum value of $I^{(i)}(k)$ of 1 *T*′ MoSSe, located around the $\pm\Lambda$ points, is larger by orders-of-magnitude than that of 2*H* MoSSe. This indicates that *k*-points near the $\pm\Lambda$ points, which are influenced by topological enhancement, make major contributions to the total susceptibility even at $\omega = 1$ eV. Note that the bandgap of 1 *T*′ MoSSe is on the order of 10 meV, and thus interband transitions of electrons near the $\pm\Lambda$ points are far off-resonance with $\omega = 1$ eV photons. However, the contributions near the $\pm\Lambda$ points still dominate those at other *k*-points where resonant interband transitions could happen. This again suggests the importance of the topological enhancement and the large interband transition dipoles near the $\pm\Lambda$ points. The topological enhancement gradually decays at large $\omega$. Consequently, the optical responses could be stronger in 2*H* MoSSe with $\omega \gtrsim 1$ eV. Other in-plane elements of the SHG tensor are shown in Supplementary Fig. 14. We also note that the theoretical calculations here should only be considered as qualitative estimations, and several issues can lead to inaccuracies. For example, the density functional theory calculations suffer from intrinsic errors regarding some electronic properties, including bandgaps. Some many-body interactions are also ignored in the calculations here. Besides, the theoretical calculations deal with ideal materials, which should be distinguished from the real samples used in experimental that are influenced by doping levels, etc. Future theoretical and experimental developments could yield more accurate information for quantitative theory-experiment comparison.

## Discussion

The giant nonlinearities of 1 *T*′ JTMD, corroborated by both experimental and theoretical results above, support the giant THz frequency photocurrent responses of 1 *T*′ JTMDs predicted by theory[3] and prelude that 1 *T*′ JTMD could serve as efficient dark-current-free THz detectors via the nonlinear bulk photovoltaic effect[10]. Our calculations indicate that the intrinsic photo-responsivity and noise equivalent power of the 1 *T*′ JTMD THz detector can outperform many current room-temperature THz sensors based on Schottky diodes or silicon field-effect transistors[40,41], albeit lower than the best pyroelectric detectors and bolometers[40] (Fig. 4g, see also Supplementary Note 1 and Supplementary Fig. 11). We foresee stacking multiple monolayer 1 *T*′ JTMDs and using field-enhancement structures[42] can further enhance the responsivity[43] and enable a facile usage of this detector for THz sensing purposes.

In conclusion, we demonstrate giant nonlinear responses in monolayer 1 *T*′ MoSSe, a prototype Janus topological semiconductor. Comparative experiments with different crystal phases (2*H* vs. 1 *T*′) and symmetry types (Janus vs. non-Janus) indicate that 1 *T*′ MoSSe possesses orders-of-magnitude enhancement in HHG and second-order THz emission efficiency, and a few times enhancement in infrared SHG. Supported by theoretical calculations, our results elucidate that the remarkable enhancements originate from augmented structural

asymmetry in Janus-type structures and topological band-mixing in 1 $T'$ phases. The boosted HHG efficiency and the high fabrication versatility[27] of 1 $T'$ JTMDs prelude a plethora of applications in lightwave electronics[44,45] in the monolayer limit. Meanwhile, the giant THz-frequency nonlinearities observed in this work could enable THz detection[46,47] with a large photo-responsivity at sub-A/W level and noise equivalent power down to the pW/$\sqrt{\text{Hz}}$ level.

## Methods

### Growth of 1 T′ $MoS_2$ monolayer flakes

The precursor $K_2MoS_4$ was prepared according to the previously reported synthesis procedures[48]. The growth of 1 $T'$ $MoS_2$ monolayer flakes was carried out in a standard CVD furnace with a 1-inch quartz tube under atmospheric pressure. A fresh-cleaved fluorophlogopite mica substrate with $K_2MoS_4$ powders were placed in the center of the furnace. After the system was purged with Ar for 10 min, the furnace was heated up to 750 °C in 40 min with 100 sccm Ar. When the temperature of the furnace reached 750 °C, 10 sccm $H_2$ was introduced and the flow rate of Ar was decreased to 90 sccm. After 5 min, the mica substrate was rapidly pulled out of the furnace heating zone. After cooling down to room temperature, the 1 $T'$ $MoS_2$ monolayer flakes were obtained.

### Synthesis of 1 T′ MoSSe monolayer flakes

The synthesis of monolayer 1 $T'$ MoSSe is realized by a room-temperature atomic layer substitution method[27] from 1 $T'$ $MoS_2$[49]. A remote commercial inductively coupled plasma (ICP) system was used to substitute the top-layer sulfur atoms of monolayer 1 $T'$ $MoS_2$ with selenium. The potassium-assisted CVD-grown monolayer 1 $T'$ $MoS_2$ was placed in the middle of a quartz tube. The plasma coil placed at the upstream of CVD furnace. The distance between the sample and the plasma coil is around 10 cm, with the selenium powder placed on the other side. At the beginning of the process, the whole system was pumped down to a low mTorr to remove air in the chamber. Then, hydrogen was introduced into the system with 10 sccm and the plasma generator was ignited for 20 min. The hydrogen atoms assist the removal of the sulfur atoms on the top layer of $MoS_2$, at the same time, the vaporized selenium filled in the vacancy of the sulfur atoms, resulting in the asymmetric Janus topological structure of MoSSe. The whole process was performed at room temperature. After the reaction, Ar gas was purged into the system with 100 sccm to remove the residual reaction gas, and the pressure was recovered to atmospheric.

### HHG, THz emission, and SHG setups

For HHG, the fundamental laser beam has a wavelength of 5.0 μm with a repetition rate of 1 kHz and a pulse duration of ~70 fs. It is generated by the difference frequency of the signal and idler beam from an optical parametric amplifier pumped with a Ti: Sapphire chirped-pulse amplifier (6 mJ, 1 kHz). The fundamental MIR beam with a 10 μJ pulse energy was focused on the sample with a ZnSe lens with a focal length of 15 cm. The measurements are performed in a transmission geometry at normal incidence. Generated HHG signals transmitted through the sample are collected by a $CaF_2$ lens and directed and dispersed in a spectrometer (Princeton Instruments HRS-300) and detected by a charge-coupled device (CCD) camera (Princeton Instruments PIXIS 400B). We note that the distorted shapes of high-order harmonics are due to chromatic aberration when focusing and imaging the HHG from the entrance slit of the spectrometer to the CCD camera.

For THz emission measurement, the ultrafast laser excitation was provided by a mode-locked Ti:Sapphire laser with pulses of 40-fs (FWHM) duration and 5.12-MHz repetition rate. After focusing the laser beam on the sample, the refocused THz radiation from the sample was detected using the electrooptic (EO) effect in a non-centrosymmetric crystal (1-mm-thick ZnTe or 258-μm-thick GaP). The induced birefringence in the EO crystal was recorded at different delay times by a laser probe pulse passing through a polarizing beamsplitter (Wollaston prism) and impinging on a balanced photodetector. The power imbalance was fed into a lock-in amplifier synchronized with modulation of the excitation beam at 320 kHz by an acousto-optic modulator. By scanning the time delay between the excitation and probe pulses, the temporal profile of the transient THz electric field could be mapped. A pair of wire-grid polarizers were used to determine the THz emission polarization.

For SHG measurement, the fundamental pulses are provided by a mode-locked Ti:Sapphire oscillator at 800-nm wavelength, 5.12-MHz repetition rate, and 40-fs pulse duration. They are focused on the sample with a ×20 objective, and the generated SHG light from a single flake is filtered and detected by a photomultiplier tube. For out-of-plane measurement, a collimated $p$-polarized pump beam with a 1 mm spot size is guided to the objective back aperture (D = 7.6 mm). The beam was focused at the sample with a tilted angle and generated an oscillating vertical electrical field to drive the out-of-plane dipole for SHG. The SHG (green) is collected with the same objective and analyzed by a polarizer. The beam position at the objective back aperture can be scanned along the $x$-direction with a motorized stage, which tunes the incident angle accordingly.

### Ab initio calculations

The ab initio density functional theory (DFT)[50,51] calculations are performed using the Vienna ab initio simulation package (VASP)[52,53]. The exchange-correlation interactions are included using generalized gradient approximation (GGA) in the form of Perdew–Burke–Ernzerhof (PBE)[54]. Core and valence electrons are respectively treated by projector augmented wave (PAW) method[55] and plane-wave basis functions. The first Brillouin zone is sampled by a 13 × 17 × 1 and 17 × 17 × 1 $k$-mesh for 1 $T'$ and 2$H$ structures, respectively.

### Nonlinear optical susceptibility calculations

After the DFT results are obtained, a tight-binding (TB) Hamiltonian in the Wannier basis is built using the Wannier90 package[56]. The TB Hamiltonian is then used to interpolate the relevant properties on a denser $k$-mesh.

The first-order susceptibility is calculated within the velocity gauge

$$\chi^{(1)}_{ij}(\omega;\omega) = -\frac{e^2}{\varepsilon_0\omega}\int\frac{d^3\boldsymbol{k}}{(2\pi)^3}\sum\nolimits_{mn}\frac{f_{mn}}{E_{mn}}\frac{v^i_{nm}v^j_{mn}}{E_{mn}-\hbar\omega} \tag{1}$$

Here $m$,$n$ label the electron states, while $v^i_{mn} \equiv \langle m|v^i|n\rangle$ is the velocity operator. $E_{mn}$ and $f_{mn}$ are respectively the difference in energy and occupation number between $|m\rangle$ and $|n\rangle$. $\varepsilon_0$ is the vacuum permittivity. The second-order susceptibility is calculated within the length gauge[57]

$$\chi^{(2)}_{ijk}(2\omega;\omega,\omega) = \zeta^{II}_{ijk}(2\omega;\omega,\omega) + \eta^{II}_{ijk}(2\omega;\omega,\omega) + \sigma^{II}_{ijk}(2\omega;\omega,\omega) \tag{2}$$

where

$$\zeta^{II}_{ijk}(2\omega;\omega,\omega) = \frac{e^3}{\varepsilon_0}\int\frac{d^3\boldsymbol{k}}{(2\pi)^3}\sum\nolimits_{mnl}\frac{r^i_{nm}r^j_{ml}r^k_{ln}}{E_{ln}-E_{ml}}\left(\frac{f_{ml}}{E_{ml}-\hbar\omega}+\frac{f_{ln}}{E_{ln}-\hbar\omega}+\frac{2f_{nm}}{E_{mn}-\hbar\omega}\right) \tag{3}$$

$$\eta^{II}_{ijk}(2\omega;\omega,\omega) = \frac{e^3}{\varepsilon_0}\int\frac{d^3\boldsymbol{k}}{(2\pi)^3}\left\{\sum\nolimits_{mnl}E_{mn}r^i_{nm}\left\{r^j_{ml}r^k_{ln}\right\}\left[\frac{f_{nl}}{E^2_{ln}(E_{ln}-\hbar\omega)}+\frac{f_{lm}}{E^2_{ml}(E_{ml}-\hbar\omega)}\right]\right.$$
$$\left.-8i\hbar\sum\nolimits_{nm}\frac{f_{nm}r^i_{nm}}{E^2_{mn}(E_{mn}-2\hbar\omega)}\left\{\Delta^j_{mn}r^k_{mn}\right\}-2\sum\nolimits_{nml}f_{nm}r^i_{nm}\frac{\left\{r^j_{ml}r^k_{ln}\right\}(\omega_{ln}-\omega_{ml})}{E^2_{mn}(E_{mn}-2\hbar\omega)}\right\} \tag{4}$$

$$\sigma^{II}_{ijk}(2\omega;\omega,\omega)=\frac{e^3}{2\varepsilon_0}\int\frac{d^3\boldsymbol{k}}{(2\pi)^3}\left\{\sum_{nml}\frac{f_{nm}}{E^2_{mn}(E_{mn}-\hbar\omega)}\left[E_{nl}r^i_{lm}\left\{r^j_{mn}r^k_{nl}\right\}-E_{lm}r^i_{nl}\left\{r^j_{lm}r^k_{mn}\right\}\right]+i\hbar\sum_{nm}\frac{f_{nm}r^i_{nm}}{E^2_{mn}\left(E_{mn}-2\hbar\omega\right)}\left\{\Delta^j_{mn}r^k_{mn}\right\}\right\} \tag{5}$$

Here the inter-band position matrix is $r^i_{mn}=\frac{\hbar v^i_{mn}}{iE_{mn}}$ for $m\neq n$ and $r^i_{mn}=0$ for $m=n$. $\Delta^i_{mn}\equiv v^i_{mm}-v^i_{nn}$ is the difference in band velocities. Meanwhile, for two numbers $A$ and $B$ one has $\{AB\}\equiv\frac{1}{2}(AB+BA)$.

The ab initio theory for calculating the third-order susceptibility is not well-developed. Here we use the velocity gauge formula[58]

$$\chi^{(3)}_{ijkl}(3\omega;\omega,\omega,\omega)=\frac{ie^4}{4\varepsilon_0\omega^3}\int\frac{d^3\boldsymbol{k}}{(2\pi)^3}\sum_{nmpq}\frac{v^i_{nm}}{E_{mn}-3\hbar\omega}\left[\frac{v^j_{mp}\left(g^l_{qn}v^k_{pq}-g^l_{pq}v^k_{qn}\right)}{E_{pn}-2\hbar\omega}+\frac{v^j_{qn}\left(g^l_{mp}v^k_{pq}-g^l_{pq}v^k_{mp}\right)}{E_{mq}-2\hbar\omega}\right] \tag{6}$$

Here $g^i_{mn}\equiv\frac{f_{nm}v^i_{mn}}{E_{nm}-\hbar\omega}$. Equation (6) experiences a spurious divergence in the real part of $\chi^{(3)}_{ijkl}$. Therefore, we first calculate the imaginary part of $\chi^{(3)}_{ijkl}$, and then obtain the real part from the Kramers–Kronig relations[59].

The $\boldsymbol{k}$-resolved contributions to the total susceptibility $I^{(i)}(\boldsymbol{k})$, which are shown in the inset of Fig. 4b–d, are defined as the integrand of the Brillouin zone integration in Eqs. (1, 2, 6). The Brillouin zone integrations is performed by a $\boldsymbol{k}$-mesh sampling, $\int\frac{d^3\boldsymbol{k}}{(2\pi)^3}=\frac{1}{V}\sum_{\boldsymbol{k}}w_{\boldsymbol{k}}$, where $V$ is the volume of the unit cell and $w_{\boldsymbol{k}}$ is the weight factor. Since 2D materials do not have well-defined volume, we use $V=Sl_{\mathrm{eff}}$, where $S$ is the area of the 2D unit cell, while $l_{\mathrm{eff}}$ is taken as 6 A for all materials. The convergence in the $\boldsymbol{k}$-mesh is tested.

## Data availability

Relevant data supporting the key findings of this study are available within the article and the Supplementary Information file. All raw data generated during the current study are available from the corresponding authors upon request.

## References


1. Choi, T. et al. Switchable ferroelectric diode and photovoltaic effect in $BiFeO_3$. *Science* **324**, 63–66 (2009).
2. Grinberg, I. et al. Perovskite oxides for visible-light-absorbing ferroelectric and photovoltaic materials. *Nature* **503**, 509–512 (2013).
3. Xu, H. et al. Colossal switchable photocurrents in topological Janus transition metal dichalcogenides. *NPJ Comput. Mater.* **7**, 31 (2021).
4. Wang, H. & Qian, X. Ferroicity-driven nonlinear photocurrent switching in time-reversal invariant ferroic materials. *Sci. Adv.* **5**, 8 (2019).
5. Sun, Z. et al. Giant nonreciprocal second-harmonic generation from antiferromagnetic bilayer $CrI_3$. *Nature* **572**, 497–501 (2019).
6. Wang, H. & Qian, X. Electrically and magnetically switchable nonlinear photocurrent in PT-symmetric magnetic topological quantum materials. *NPJ Comput. Mater.* **6**, 1–8 (2020).
7. Orenstein, J. et al. Topology and symmetry of quantum materials via nonlinear optical responses. *Annu. Rev. Condens. Matter Phys.* **12**, 247–272 (2021).
8. Xu, H., Wang, H., Zhou, J. & Li, J. Pure spin photocurrent in non-centrosymmetric crystals: bulk spin photovoltaic effect. *Nat. Commun.* **12**, 4330 (2021).
9. Morimoto, T. & Nagaosa, N. Topological nature of nonlinear optical effects in solids. *Sci. Adv.* **2**, 5 (2016).
10. Zhang, Y. & Fu, L. Terahertz detection based on nonlinear Hall effect without magnetic field. *Proc. Natl. Acad. Sci. USA* **118**, e2100736118 (2021).
11. Wu, L. et al. Giant anisotropic nonlinear optical response in transition metal monopnictide Weyl semimetals. *Nat. Phys.* **13**, 350–355 (2017).
12. Osterhoudt, G. B. et al. Colossal mid-infrared bulk photovoltaic effect in a type-I Weyl semimetal. *Nat. Mater.* **18**, 471–475 (2019).
13. Ma, J. et al. Nonlinear photoresponse of type-II Weyl semimetals. *Nat. Mater.* **18**, 476–481 (2019).
14. Mrudul, M. S., Jiménez-Galán, Á., Ivanov, M. & Dixit, G. Light-induced valleytronics in pristine graphene. *Optica* **8**, 422–427 (2021).
15. Schmid, C. et al. Tunable non-integer high-harmonic generation in a topological insulator. *Nature* **593**, 385–390 (2021).
16. Heide, C. et al. Probing topological phase transitions using high-harmonic generation. *Nat. Photon.* **16**, 620–624 (2022).
17. Bai, Y. et al. High-harmonic generation from topological surface states. *Nat. Phys.* **17**, 311–315 (2021).
18. Bharti, A., Mrudul, M. S. & Dixit, G. High-harmonic spectroscopy of light-driven nonlinear anisotropic anomalous Hall effect in a Weyl semimetal. *Phys. Rev. B* **105**, 155140 (2022).
19. Okamura, Y. et al. Giant magneto-optical responses in magnetic Weyl semimetal $Co_3Sn_2S_2$. *Nat. Commun.* **11**, 4619 (2020).
20. Hafez, H. et al. Extremely efficient terahertz high-harmonic generation in graphene by hot Dirac fermions. *Nature* **561**, 507–511 (2018).
21. Yin, X. et al. Edge nonlinear optics on a $MoS_2$ atomic monolayer. *Science* **344**, 488–490 (2014).
22. Qian, X., Liu, J., Fu, L. & Li, J. Quantum spin Hall effect in two-dimensional transition metal dichalcogenides. *Science* **346**, 1344–1347 (2014).
23. Keum, D. H. et al. Bandgap opening in few-layered monoclinic $MoTe_2$. *Nat. Phys.* **11**, 482–486 (2015).
24. Tang, S. et al. Quantum spin Hall state in monolayer 1*T*′-$WTe_2$. *Nat. Phys.* **13**, 683–687 (2017).
25. Lu, A.-Y. et al. Janus monolayers of transition metal dichalcogenides. *Nat. Nanotechnol.* **12**, 744–749 (2017).
26. Li, R., Cheng, Y. & Huang, W. Recent progress of Janus 2D transition metal chalcogenides: from theory to experiments. *Small* **14**, 1802091 (2018).
27. Guo, Y. et al. Designing artificial two-dimensional landscapes via atomic-layer substitution. *Proc. Natl. Acad. Sci. USA* **118**, e2106124118 (2021).
28. Yang, Y. et al. High-efficiency light-emitting devices based on quantum dots with tailored nanostructures. *Nat. Photonics* **9**, 259–266 (2015).
29. Ghimire, S. et al. Observation of high-order harmonic generation in a bulk crystal. *Nat. Phys.* **7**, 138–141 (2011).
30. Liu, H. et al. High-harmonic generation from an atomically thin semiconductor. *Nat. Phys.* **13**, 262–265 (2017).
31. Liu, F. et al. Disassembling 2D van der Waals crystals into macroscopic monolayers and reassembling into artificial lattices. *Science* **367**, 903–906 (2020).
32. Ma, E. et al. Recording interfacial currents on the subnanometer length and femtosecond time scale by terahertz emission. *Sci. Adv.* **5**, 2 (2019).
33. Fan, Z. et al. Terahertz surface emission from $MoSe_2$ at the monolayer limit. *ACS Appl. Mater. Interfaces* **12**, 48161–48169 (2020).
34. Kumar, N. et al. Second harmonic microscopy of monolayer $MoS_2$. *Phys. Rev. B* **87**, 161403 (2013).
35. Janisch, C. et al. Extraordinary second harmonic generation in tungsten disulfide monolayers. *Sci. Rep.* **4**, 5530 (2015).
36. Li, Y. et al. Probing symmetry properties of few-layer $MoS_2$ and h-BN by optical second-harmonic generation. *Nano Lett.* **13**, 3329–3333 (2013).

37. de Juan, F., Grushin, A. G., Morimoto, T. & Moore, J. E. Quantized circular photogalvanic effect in Weyl semimetals. *Nat. Commun.* **8**, 15995 (2017).
38. Xu, H., Zhou, J., Wang, H. & Li, J. Giant photonic response of Mexican-hat topological semiconductors for mid-infrared to terahertz applications. *J. Phys. Chem. Lett.* **11**, 6119–6126 (2020).
39. Tan, L. Z. & Rappe, A. M. Enhancement of the bulk photovoltaic effect in topological insulators. *Phys. Rev. Lett.* **116**, 237402 (2016).
40. Lewis, R. A. A review of terahertz detectors. *J. Phys. D Appl. Phys.* **52**, 433001 (2019).
41. Sizov, F. & Rogalski, A. THz detectors. *Prog. Quantum. Electron.* **34**, 278–347 (2010).
42. Chen, H.-T. et al. Active terahertz metamaterial devices. *Nature* **444**, 597–600 (2006).
43. Zhao, Y.-F. et al. Tuning the Chern number in quantum anomalous Hall insulators. *Nature* **588**, 419–423 (2020).
44. Reimann, J. et al. Subcycle observation of lightwave-driven Dirac currents in a topological surface band. *Nature* **562**, 396–400 (2018).
45. Higuchi, T., Heide, C., Ullmann, K., Weber, H. B. & Hommelhoff, P. Light-field-driven currents in graphene. *Nature* **550**, 224–228 (2017).
46. Cai, X. et al. Sensitive room-temperature terahertz detection via the photothermoelectric effect in graphene. *Nat. Nanotechnol.* **9**, 814–819 (2014).
47. Vicarelli, L. et al. Graphene field-effect transistors as room-temperature terahertz detectors. *Nat. Mater.* **11**, 865–871 (2012).
48. Cordova, A., Blanchard, P., Lancelot, C., Frémy, G. & Lamonier, C. Probing the nature of the active phase of molybdenum-supported catalysts for the direct synthesis of methylmercaptan from syngas and $H_2S$. *ACS Catal.* **5**, 2966–2981 (2015).
49. Liu, L. et al. Phase-selective synthesis of 1*T*′ $MoS_2$ monolayers and heterophase bilayers. *Nat. Mater.* **17**, 1108–1114 (2018).
50. Hohenberg, P. & Kohn, W. Inhomogeneous electron gas. *Phys. Rev.* **136**, B864–B871 (1964).
51. Kohn, W. & Sham, L. J. Self-consistent equations including exchange and correlation effects. *Phys. Rev.* **140**, A1133–A1138 (1965).
52. Kresse, G. & Furthmüller, J. Efficiency of ab-initio total energy calculations for metals and semiconductors using a plane-wave basis set. *Comput. Mater. Sci.* **6**, 15–50 (1996).
53. Kresse, G. & Furthmüller, J. Efficient iterative schemes for ab initio total-energy calculations using a plane-wave basis set. *Phys. Rev. B* **54**, 11169–11186 (1996).
54. Perdew, J. P., Burke, K. & Ernzerhof, M. Generalized gradient approximation made simple. *Phys. Rev. Lett.* **77**, 3865–3868 (1996).
55. Blöchl, P. E. Projector augmented-wave method. *Phys. Rev. B* **50**, 17953–17979 (1994).
56. Mostofi, A. A. et al. An updated version of wannier90: a tool for obtaining maximally-localised Wannier functions. *Comput. Phys. Commun.* **185**, 2309–2310 (2014).
57. Sipe, J. E. & Shkrebtii, A. I. Second-order optical response in semiconductors. *Phys. Rev. B* **61**, 5337–5352 (2000).
58. Taghizadeh, A., Hipolito, F. & Pedersen, T. G. Linear and nonlinear optical response of crystals using length and velocity gauges: effect of basis truncation. *Phys. Rev. B* **96**, 195413 (2017).
59. Hutchings, D. C., Sheik-Bahae, M., Hagan, D. J. & Van Stryland, E. W. Kramers-Krönig relations in nonlinear optics. *Opt. Quant. Electron.* **24**, 1–30 (1992).


## Acknowledgements

This work was primarily funded through the Department of Energy, Office of Basic Energy Sciences, Division of Materials Sciences and Engineering, under contract DE-AC02-76SF00515. The high harmonic generation experiments were supported by the US Department of Energy, Office of Science, Basic Energy Sciences, Chemical Sciences, Geosciences, and Biosciences Division through the AMOS program. Y.G. acknowledges the financial support from Zhejiang University. H.X. and J.L. were supported by an Office of Naval Research MURI through grant #N00014-17-1-2661. E.S. and H.S. acknowledge the financial support from Research Center for Industries of the Future at Westlake University, National Natural Science Foundation of China (grant no. 52272164). J.K. and T.Z. acknowledge the financial support from US Department of Energy (DOE), Office of Science, Basic Energy Sciences under Award DE-SC0020042.

## Author contributions

J.S., H.X., Y.G. and A.L. designed the study; Y.G. performed the Janus material synthesis and Raman characterization; H.X. and J.L. performed the theoretical analyses and ab initio calculations.; C.H. and J.S. performed HHG measurements under the supervision of S.G. and A.L.; C.X. and J.S. performed TES measurements under the supervision of A.L.; C.H.F. synthesized typical transition metal dichalcogenides under the supervision of L.J.; J.S., F.Q. and L.Y. performed SHG measurements under the supervision of A.L. and T.H.; A.J. synthesized wafer-scale 2H MoS2 under the supervision of F.L.; H.S., T.Z., E.S. and J.K. participated in data analysis; J.S., H.X. and Y.G. wrote the manuscript; All authors read and revised the manuscript.

## Competing interests

The authors declare no competing interests.

## Additional information

**Supplementary information** The online version contains supplementary material available at https://doi.org/10.1038/s41467-023-40373-z.

**Correspondence** and requests for materials should be addressed to Yunfan Guo or Aaron M. Lindenberg.

**Peer review information** *Nature Communications* thanks Sebastian Maehrlein, Gopal Dixit and the other, anonymous, reviewer(s) for their contribution to the peer review of this work. A peer review file is available.

**Supplementary Information**

# Giant room-temperature nonlinearities in a monolayer Janus topological semiconductor

Jiaojian Shi[1,2,†], Haowei Xu[3,†],Christian Heide[4,5], Changan HuangFu[6], Chenyi Xia[1,2], Felipe de Quesada[1,2], Hongzhi Shen[7], Tianyi Zhang[8], Leo Yu[9], Amalya Johnson[1], Fang Liu[5,10], Enzheng Shi[7], Liying Jiao[6], Tony Heinz[5,9], Shambhu Ghimire[5], Ju Li[3,11], Jing Kong[8], Yunfan Guo[12*], Aaron M. Lindenberg[1,2,5*]

[1]Department of Materials Science and Engineering, Stanford University, Stanford, California 94305, United States

[2]Stanford Institute for Materials and Energy Sciences, SLAC National Accelerator Laboratory, Menlo Park, California 94025, United States

[3]Department of Nuclear Science and Engineering, Massachusetts Institute of Technology, Cambridge, Massachusetts 02139, United States

[4]Department of Applied Physics, Stanford University, Stanford, California 94305, United States

[5]Stanford PULSE Institute, SLAC National Accelerator Laboratory, Menlo Park, California 94025, United States

[6]Key Laboratory of Organic Optoelectronics and Molecular Engineering of the Ministry of Education, Department of Chemistry, Tsinghua University, Beijing 100083, China

[7]School of Engineering, Westlake University, Hangzhou, 310024, China

[8]Department of Electrical Engineering and Computer Science, Massachusetts Institute of Technology, Cambridge, Massachusetts 02139, United States

[9]E. L. Ginzton Laboratory, Stanford University, Stanford, California 94305, United States

[10]Department of Chemistry, Stanford University, Stanford, California 94305, United States

[11]Department of Materials Science and Engineering, Massachusetts Institute of Technology, Cambridge, Massachusetts 02139, United States

[12]Key Laboratory of Excited-State Materials of Zhejiang Province, Department of Chemistry, State Key Laboratory of Silicon and Advanced Semiconductor Materials, Zhejiang University, Hangzhou 310058, China

*Corresponding author. E-mail: yunfanguo@zju.edu.cn (Y. G.); aaronl@stanford.edu (A. L.)

[†]These authors contributed equally to this work.

**Supplementary Note 1. Estimation of photo-responsivity and noise-equivalent power of THz detectors based on 1$T'$ JTMD**

The photo-responsivity of the THz detector is defined as the DC photo-current $I_{\mathrm{DC}}$ divided by the absorbed THz power $P_{\mathrm{abs}}$

$$\mathcal{r} = \frac{I_{\mathrm{DC}}}{P_{\mathrm{abs}}} \quad \text{(Supplementary Equation 1)}$$

Using the geometry shown in Fig. S11, the DC current can be expressed as

$$I_{\mathrm{DC}} = \frac{1}{2}\xi(\omega)E^2 wd \quad \text{(Supplementary Equation 2)}$$

where $E$ is the electric field strength of the incident THz radiation. $\xi(\omega)$ is the second-order photoconductivity (e.g., the shift current conductivity). From our ab initio calculations, $\xi(\omega)d$ of 1$T'$ JTMD is on the order of $10^3$ nm · μA/V$^2$ in the THz range[1]. Meanwhile, the absorbed power of the 2D flake is[2]

$$\begin{aligned} P_{\mathrm{abs}} &= P_0\left[1-\exp\left(-\frac{\sigma_r(\omega)d}{c_0\varepsilon_0}\right)\right] \\ &\approx P_0\frac{\sigma_r(\omega)d}{c_0\varepsilon_0} \end{aligned} \quad \text{(Supplementary Equation 3)}$$

Here $P_0 = \frac{1}{2}c_0\varepsilon_0E^2wl$ is the incident power, $c_0$ is the speed of light, and $\varepsilon_0$ is the vacuum permittivity. $\sigma_r(\omega)$ is the real part of the first-order conductivity, and one has $\sigma_r(\omega)d \sim 5\times10^4$ nm · S/m in the THz range, according to our ab initio calculations. Then, one has the photo-responsivity of the 1$T'$ JTMD THz detector as

$$\mathcal{r}(\omega) = \frac{I_{\mathrm{DC}}}{P_{\mathrm{abs}}} = \frac{\xi(\omega)}{\sigma_r(\omega)l} \sim 0.2\ \mathrm{A/W} \quad \text{(Supplementary Equation 4)}$$

as shown in Fig. 4 in the main text. Here we used[3,4] $l = 0.1$ μm.

Next, we estimate the noise-equivalent power (NEP) of the 1$T'$ JTMD THz detector, which can be obtained from

$$\mathrm{NEP} = \frac{\sqrt{4k_BT/R_0}}{\mathcal{r}}, \quad \text{(Supplementary Equation 5)}$$

where $k_B$ is the Boltzmann constant, $T$ is the temperature. The resistance of the JTMD sample can be estimated with

$$R_0 = \frac{1}{\sigma_r(\omega=0)}\frac{l}{wd} \approx 2\times10^4\ \Omega, \quad \text{(Supplementary Equation 6)}$$

which is comparable with the experimental results[4] of 1$T'$ $MoS_2$. Here we used $l = w$. Finally, one has

$$\mathrm{NEP} \sim 5\ \mathrm{pW}/\sqrt{\mathrm{Hz}}$$

in the THz range (Fig. 4 in the main text).

**Supplementary Note 2. Additional information about HHG efficiency comparison with other samples**

For comparison with 17th-order HHG at ZnO, our data show similar cutoff orders and signal-to-noise ratios as the ZnO data[5] under similar incident MIR fields at ~ 0.2 V/Å despite on a monolayer flake (< 1 nm) with ~10 μm lateral sizes. The 500-μm ZnO used is theoretically shown to have an effective thickness of 100-200 nm[6], meaning the HHG efficiency per thickness at 1*T'* MoSSe is at least 100 times higher. When taking the lateral size (~10 μm) and beam spot size (~100 μm) into account, the 1*T'* MoSSe HHG could be 1000 times higher than ZnO. For 18th-order HHG, ZnO is centrosymmetric and does not generate even-order harmonics. Similar comparisons are performed for other solid samples in Table 1.

**Supplementary Note 3. Estimation of momentum change in intraband electron acceleration**

We can estimate the distance using the semi-classical equation of motion of the electrons: $\frac{\partial k}{\partial t} = \frac{eE}{\hbar}$, where $E$ is the electric field. This equation yields $\Delta k \approx \frac{\tau e E}{\hbar}$, where $\tau$ is the decoherence time of the electrons. Taking $\tau = 1$ fs and $E = 1\ \mathrm{V/nm}$, one has $\Delta k \approx 0.15\ \mathrm{Å}^{-1}$, which is $1 \sim 10$ % of the size of the Brillouin zone.

**Supplementary Note 4. Sample stability discussion under thermal and laser excitation**

From the energetic perspective, the 2H phases should be more stable than the 1T' phases, as reported in Fig. S7 in the Supplementary of Ref. [7] The 1T' phase is a metastable state, and its energy per unit cell is around $0.5$ eV higher than that of the 2H phase. From the practical perspective, the Janus structure is less stable than the non-Janus structure thermodynamically. For its stability under MIR excitation, we did not observe any evident sample damage in either 1T' or 2H phase MoSSe under the highest possible MIR fluence available in our lab.

**Supplementary Note 5. Additional discussion on the angle and fluence dependence in TES measurements**

The sinusoidal angle dependence with a period of $\pi$ shown in Fig. 3c in the main text is a typical feature of second-order nonlinear optical responses. This is because the total response is $R \sim E \cdot \chi^{(2)} \cdot E$, where $\chi^{(2)}$ is a rank-2 tensor. If the polarization of $E$ is rotated in the $x$-$y$ plane with an angle of $\theta$, then one has $R(\theta) = E^2\left[\chi_{xx}^{(2)} \cos^2\theta + \chi_{yy}^{(2)} \sin^2\theta + 2\chi_{xy}^{(2)} \sin\theta \cos\theta\right]$. Hence, the sinusoidal angle dependence appears as long as $\chi^{(2)}$ is not proportional to identity tensor. From

such angle dependence, one can assess e.g., if there is a mirror symmetry. But usually, one cannot get full information on the crystal symmetry (e.g., space group) from these angle dependences. Similar angle dependence data and microscopic origin above has been reported in Ref. [8]. For the fluence dependence data shown in Fig. 3d, the signal continues to increase at higher fluences, albeit with a smaller gradient. Such phenomena are likely due to two combined effects: (1) Saturation of photocurrents due to carrier generation, as reported in Ref. [8]; (2) Nonlinear photocurrents that leads to increasing THz emission signal as a function of excitation fields.

**Supplementary Note 6. Additional discussion on TES and SHG measurements in 2H-MoSSe and 2H-$MoS_2$**

Regarding 2H-MoSSe and 2H-$MoS_2$, they show vanishing TES signal and detectable SHG signal, which is likely due to a resonant effect. SHG concerns the sum-frequency process, which is characterized by $\chi^{(2)}(\omega, \omega; 2\omega)$, where $\omega$ is the input frequency. For 2H $MoS_2$ and MoSSe, the doubled frequency $2\omega$ (around 3 eV) is above the bandgap (below 2 eV). Consequently, the SHG can be resonantly boosted. In contrast, the TES process is characterized by $\chi^{(2)}(\omega_1, \omega_2; \omega_1 - \omega_2)$, where $\omega_1$ and $\omega_2$ are two input frequencies, while $\omega_1 - \omega_2$ is the difference frequency and is in the THz range. In our experiments, $\omega_1, \omega_2$ and $\omega_1 - \omega_2$ are all below the bandgap of 2H $MoS_2$ and MoSSe. Hence, the TES for the 2H-phase structures is basically a non-resonant process and is intrinsically weaker than the resonant SHG. In addition, the signal levels in these two independent experiments are also influenced by the different detection sensitivities for TES and SHG.

**Supplementary Note 7. Additional discussion on incident angle dependence in SHG**

The angle dependence is dominated by the crystal structure. For example, if the crystal structure is isotropic with e.g., octahedral symmetry, then there should be no angle dependence. On the other hand, if the symmetry of the crystal structure is lower, then the angle dependence can appear, because electric fields with different polarization "feels" different atomic environment, and the optical responses would be different. On the other hand, topological properties typically do not have a significant impact on angle dependence. For instance, isotropic structures, regardless of whether they possess topological properties or not, should not display any angle dependence.

**Supplementary Note 8. Additional discussion on nonlinear susceptibility calculation**

Note that the SHG of 2H MoSSe in Fig. 4e seems small because that of 1T' MoSSe is huge at small frequencies. In other words, the scale of the $y$-axis in Fig. 4 is large. The nonlinear susceptibility $\chi^{(2)}$ of the SHG of 2H MoSSe is on the order of $1\ \mathrm{nm/V}$, which is quite large (see also Supplementary Fig. 14). The SHG $\chi^{(2)}$ of typical crystals is on the order of $10^{-3}\ \mathrm{nm/V}$. We also note that the specific tensor elements shown in Fig. 4 are chosen because they are relatively large among all tensor elements. The other in-plane elements of the SHG tensor are shown in Supplementary Fig. 14.

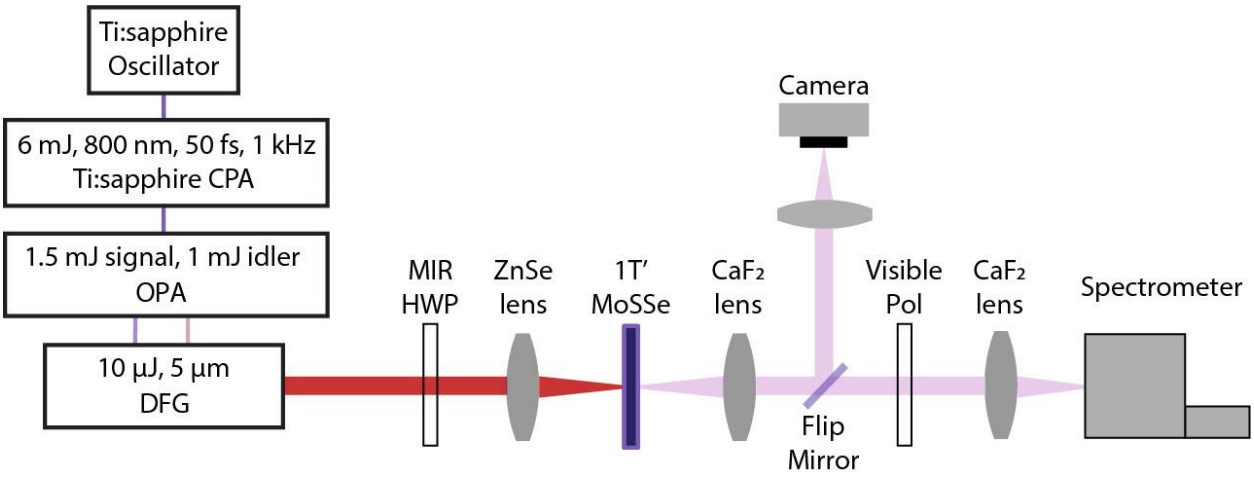


**Supplementary Fig. 1 | Schematic illustration of the HHG setup.** An amplified Ti:sapphire laser system is used to pump an optical parametric amplifier (OPA, TOPAS-HE, Light Conversion Inc.). The signal (~ 1300 nm) and idler (~ 1900 nm) from the OPA are mixed in a GaSe crystal (Eksma Optics Inc., *z*-cut, 0.5 mm thick) for difference-frequency generation. The resulting mid-infrared radiation is cleaned by a bandpass filter, centered at 5.0 $\mu$m (Thorlabs Inc., FB5000-500). The polarization of the MIR beam is controlled by a zero-order $MgF_2$ half-wave plate (HWP) and focuses on the sample with a 15 cm focal length lens. The spot sizes are 100 $\mu$m ($1/e^2$ intensity radius) for the MIR beam. A 20× Mitutoyo microscope objective attached to a CCD camera can be placed directly behind the sample to characterize the spot size at the focal plane and align the spot on the sample. The spot size of the MIR-beam is characterized with a beam profiler (Dataray, WinCamD-IR-BB). The generated high harmonics are collected and focused by $CaF_2$ lenses and directed into a spectrometer equipped with a thermoelectronically cooled CCD camera (Princeton Instruments Inc., Pixis 400B). All HHG spectra were measured in a transmission geometry and under ambient conditions.

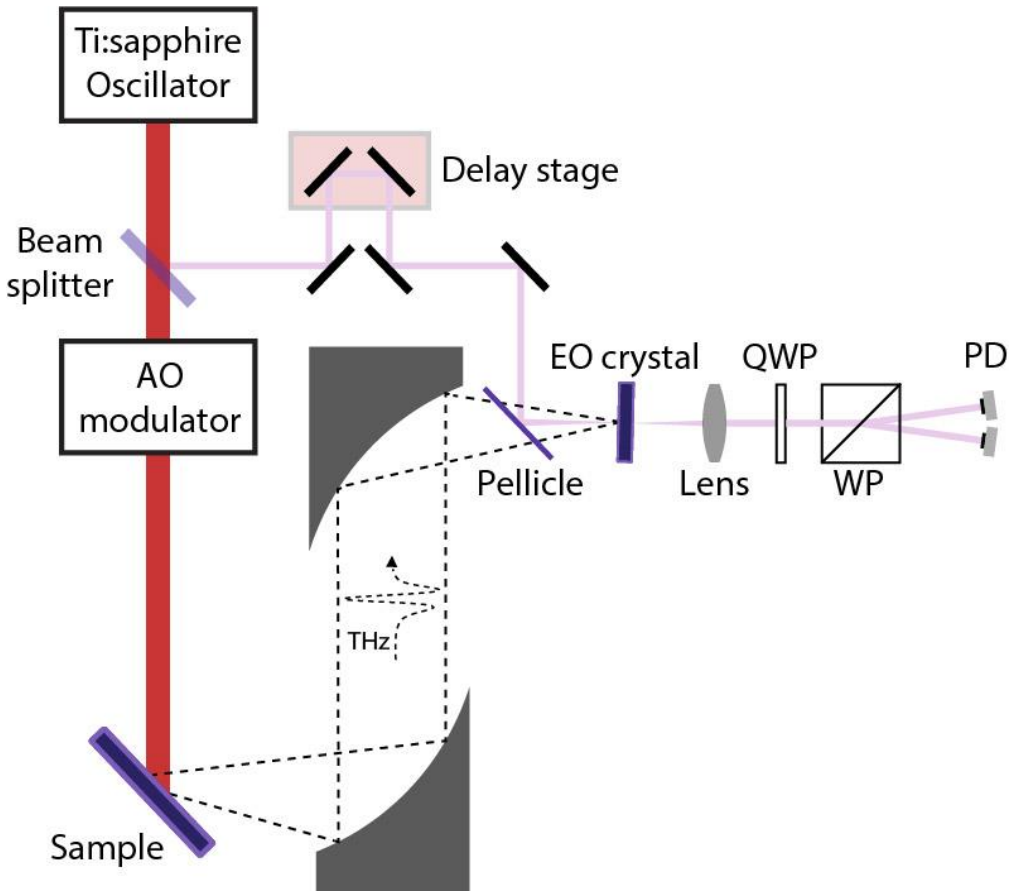


**Supplementary Fig. 2 | Schematic illustration of the TES setup.** A long-cavity Ti:sapphire oscillator (5.12 MHz repetition rate) is used to pump the sample for THz generation. The residual 800-nm beam after the sample is a 500-μm-thick high-resistivity Si wafer. The pump beam is modulated by an acousto-optic modulator for lock-in detection. The generated THz emission is focused on a electro-optic (EO) crystal, which is either a 1-mm thick ZnTe or a 258-μm-thick GaP. AO: acousto-optic, WP: Wollaston prism, PD: photodetector, QWP: quarter-wave plate.

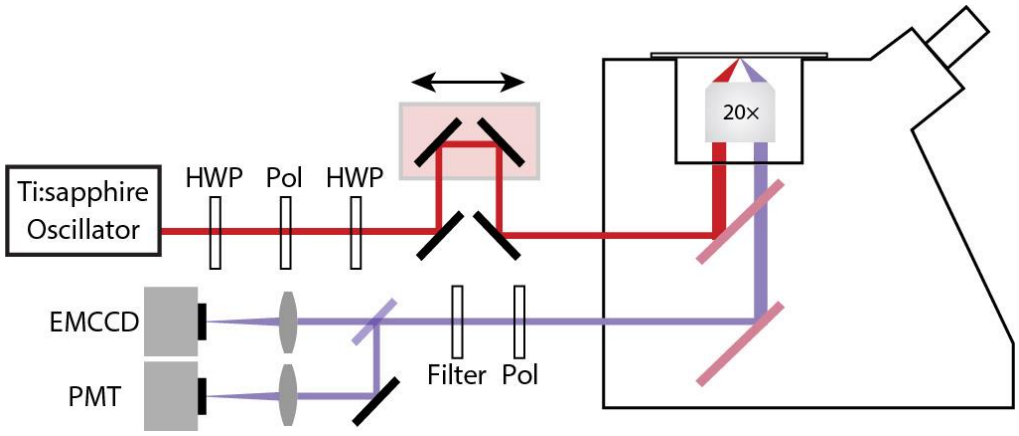


**Supplementary Fig. 3 | Schematic illustration of the angle-resolved SHG setup.** The fundamental beam is provided by a Ti:sapphire oscillator and coupled to a 20× objective for SHG measurements. The beam can be displaced perpendicular to the beam perpendicularly to the beam direction by moving the translational stage, which enables angle-resolved SHG measurements. The collected SHG signal is detected by either an electron-multiplying charge-coupled device or a photomultiplier tube.

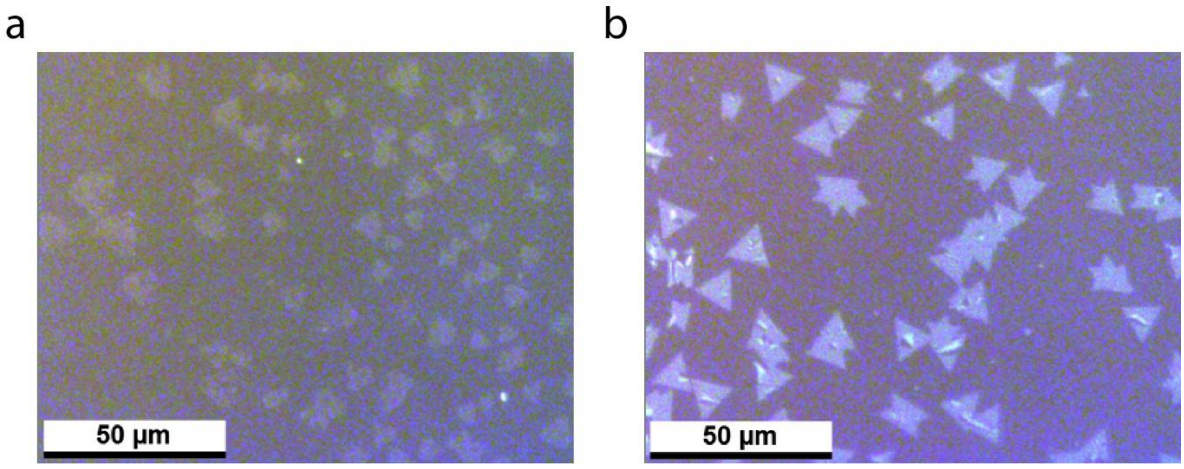


**Supplementary Fig. 4 | Optical images of 1*T′* MoSSe (left) and 2*H* MoSSe (right)**. The spacing between the flakes are randomly distributed. Experimentally, we irradiated a single flake in a sparsely populated area and confirmed that we did not experience any interference from neighboring flakes. We achieved this by measuring the polarization dependence and observing the near-perfect cancellation of HHG at specific angles to one of the crystallographic axes.

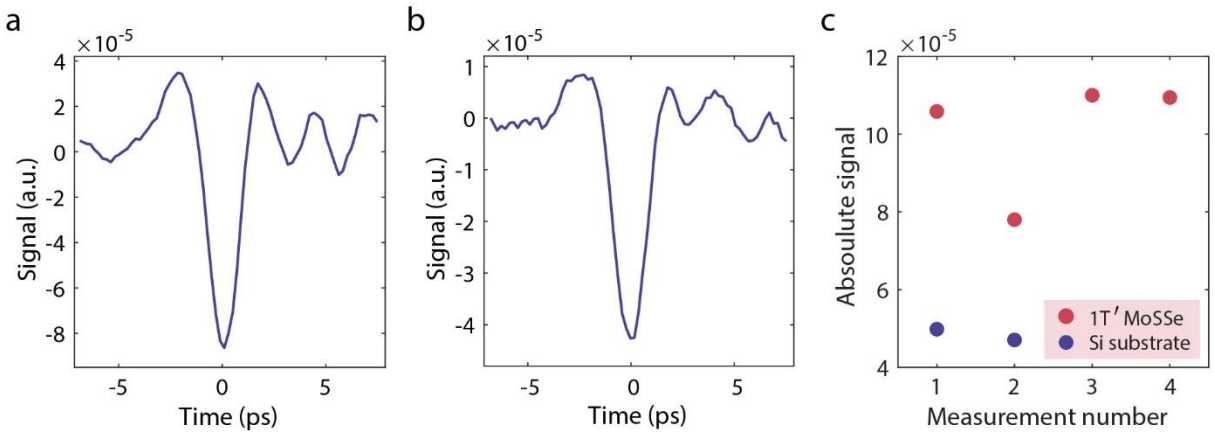


**Supplementary Fig. 5 | TES measurements on 1*T′* MoSSe grown on silicon and silicon substrate**. **a**, THz emission signal from 1*T′* MoSSe grown on silicon. It contains both signals from 1*T′* MoSSe and the silicon substrate. **b**, THz emission signal from the bare silicon substrate. **c**, Measurements on different sample spots show that THz emission intensities in 1*T′* MoSSe sample are about two times from the bare substrate, meaning the signal from 1*T′* MoSSe is comparable to those from the silicon substrate.

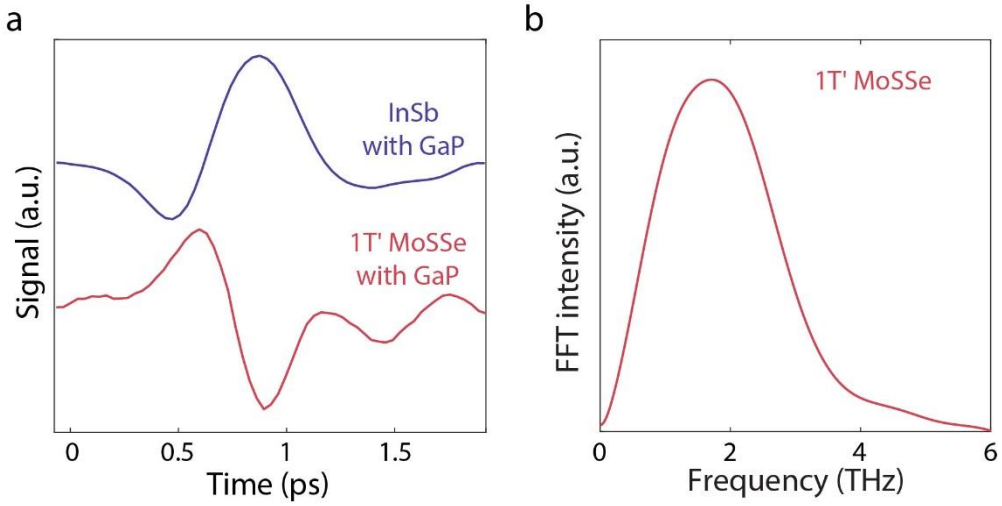


**Supplementary Fig. 6 | TES experiments on InSb and 1*T′* MoSSe measured with gallium phosphite crystal. a,** TES measurement on reference sample InSb and 1*T′* MoSSe. The EO crystal here is GaP crystal that can measure higher frequency components than the ZnTe crystal used to obtain results reported in the main text. **b**, THz emission spectrum of 1*T′* MoSSe shows a center frequency at about 1.6 THz and extends up to 4 THz.

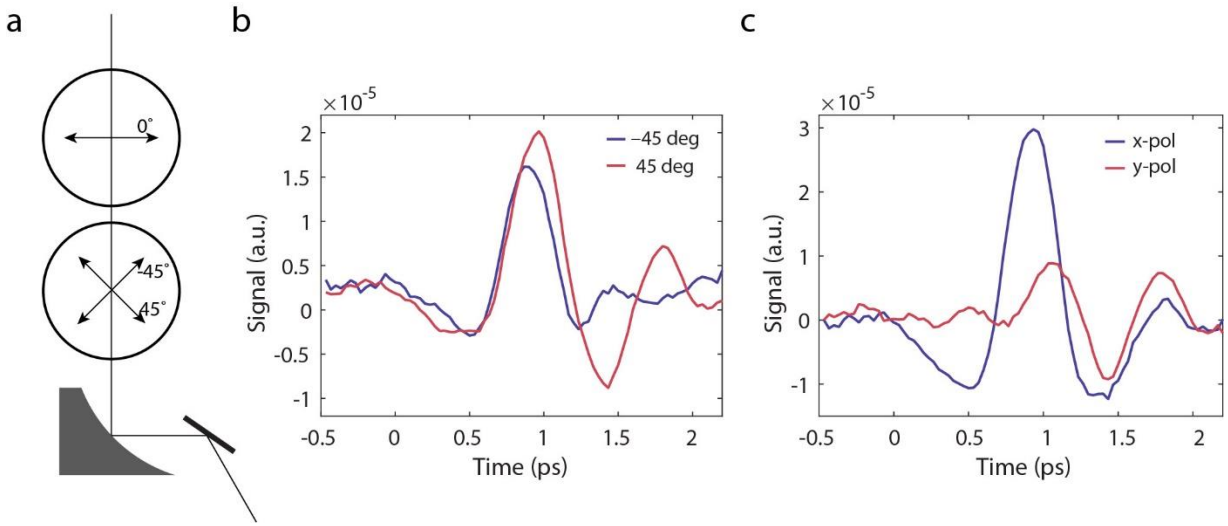


**Supplementary Fig. 7 | THz emission polarization analysis with linearly polarized 800-nm pump.** **a**, schematic illustration of THz emission polarization analysis. The polarization of the second polarizer (along the beam) was fixed to be horizontal (0 degree). The polarization of the first polarizer was chosen to be 45 degree or -45 degree for comparison. **b**, THz emission traces at 45 degree and -45 degree polarization angles. **c**, THz emission traces with *x* and *y* polarization inferred from **b**, which shows the emission is mainly polarized along the *x*-direction.

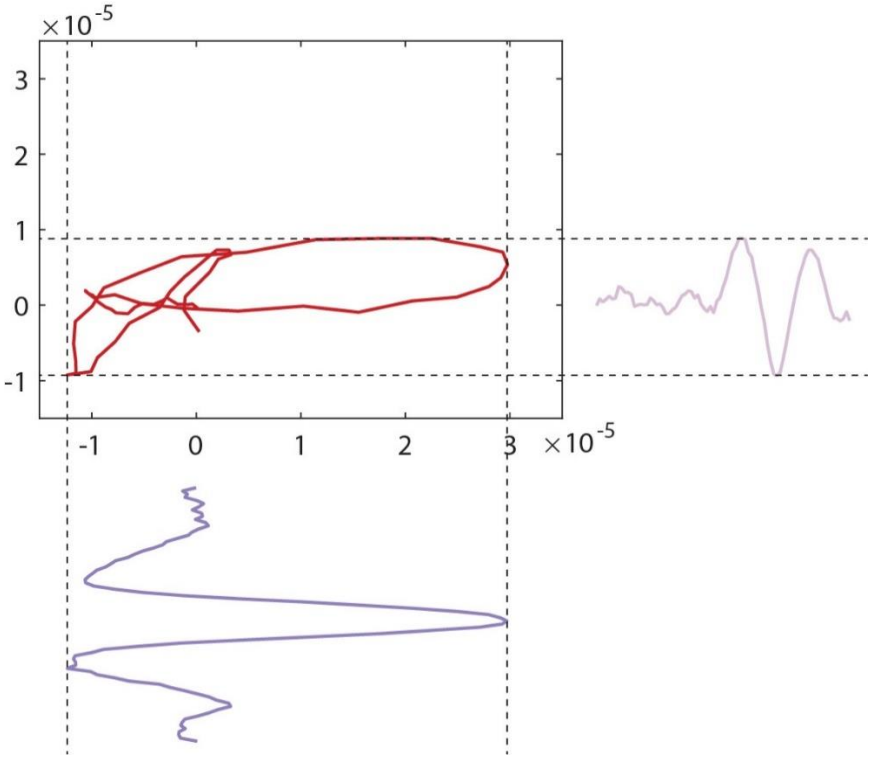


**Supplementary Fig. 8 | Lissajous curve of the THz emission pumped with a linearly polarized 800-nm beam.**

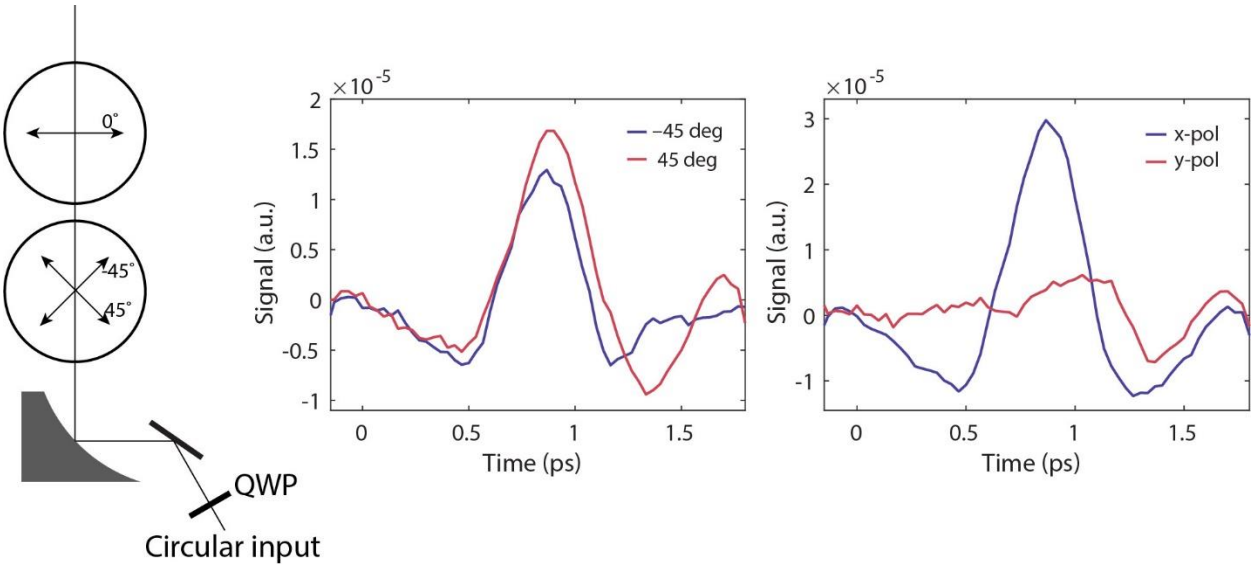


**Supplementary Fig. 9 | THz emission polarization analysis with circularly polarized 800-nm pump.** **a**, schematic illustration of THz emission polarization analysis with circularly polarized pump. **b**, THz emission traces at 45 degree and -45 degree polarization angles. **c**, THz emission traces with *x* and *y* polarization inferred from **b**, which shows the emission is mainly polarized along the *x*-direction.

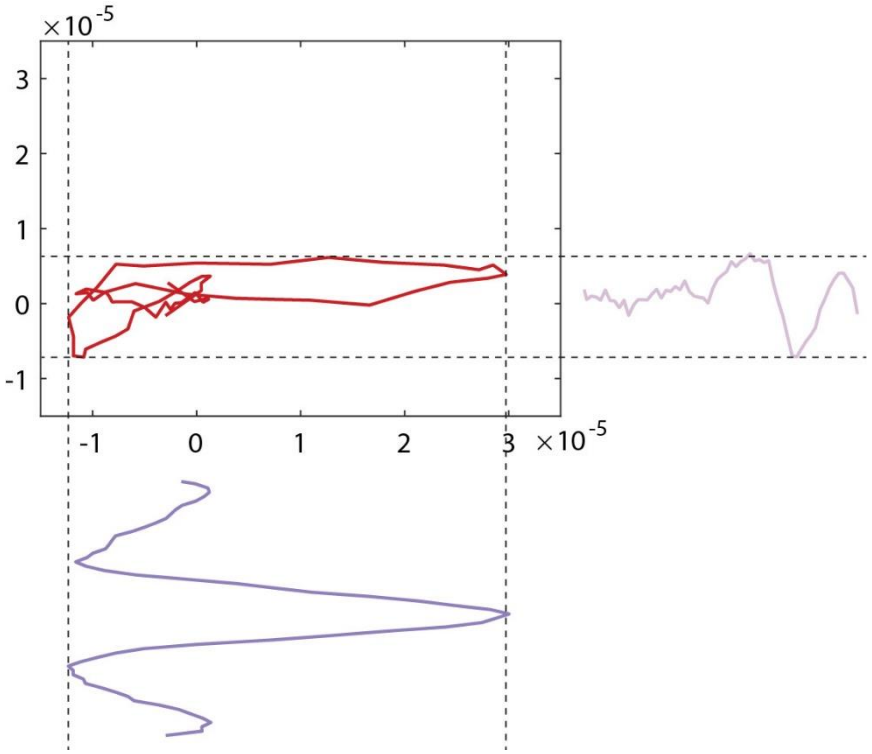


**Supplementary Fig. 10 | Lissajous curve of the THz emission pumped with a linearly polarized 800-nm beam.** It shows the emission is mainly linearly polarized and along the *x*-direction with a slight ellipticity.

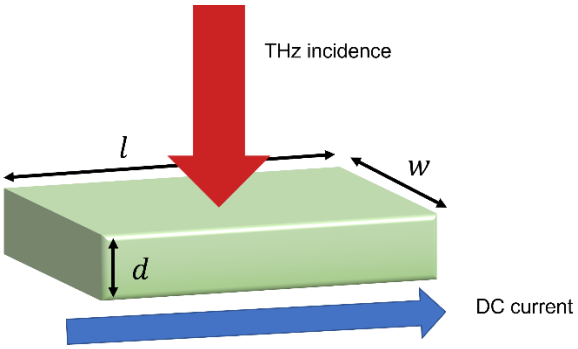


**Supplementary Fig. 11 | Sample geometry**. $l$ and $w$ are the length and width of the JTMD sample, respectively. $d$ is the thickness of the JTMD monolayer. The THz radiation is along the out-of-plane direction, while the DC current is along the in-plane direction.

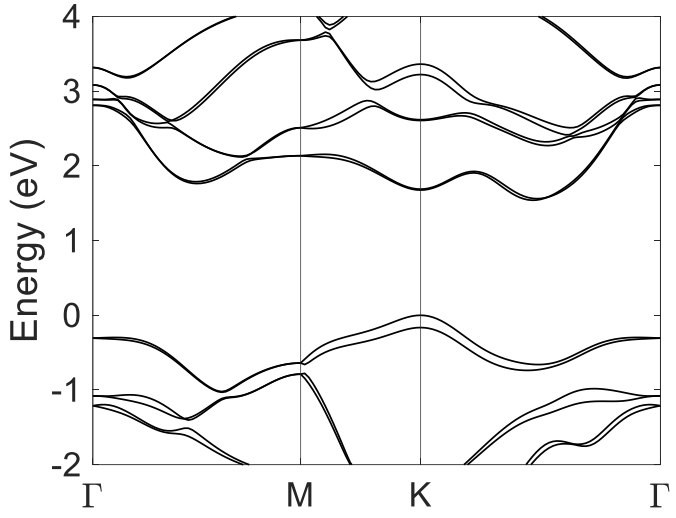


**Supplementary Fig. 12 |** Calculated electronic band structure of 2*H* MoSSe.

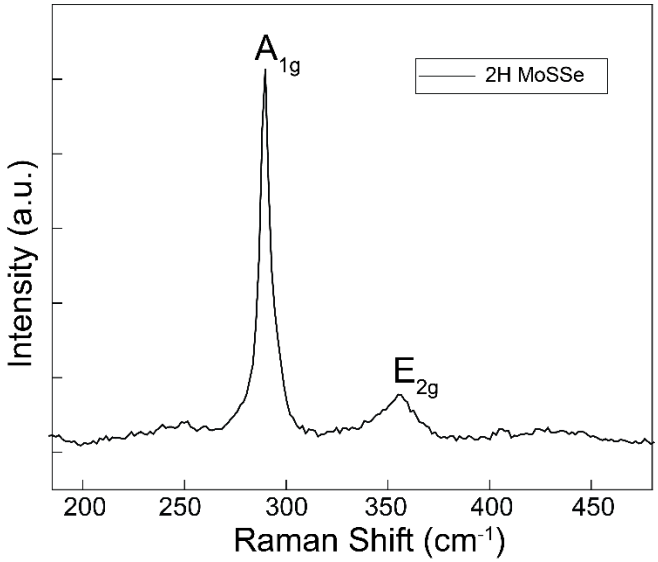


**Supplementary Fig. 13 |** Raman spectrum of 2*H* MoSSe.

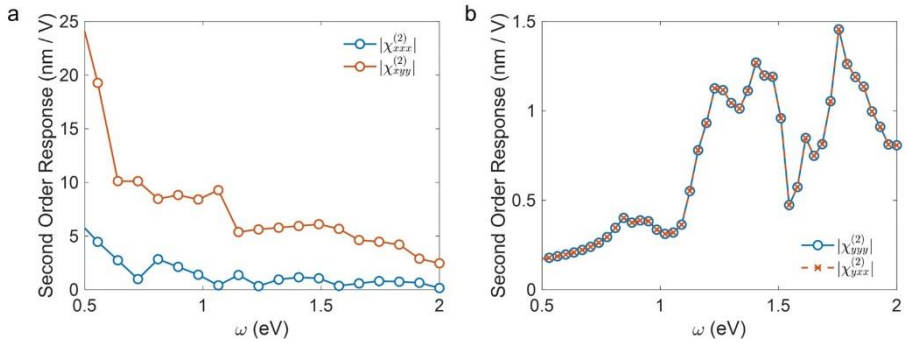


**Supplementary Fig. 14 |** Non-zero in-plane components of the SHG tensor in (**a**) 1T' and (**b**) 2H MoSSe. Other in-plane components are forbidden by mirror symmetries. In (b), the magnitude of the SHG tensor is the same for $\chi^{(2)}_{yyy}$ and $\chi^{(2)}_{yxx}$ because of the three-fold rotation symmetry in the 2H phase.

**Supplementary References**


1. Xu, H. *et al.* Colossal switchable photocurrents in topological Janus transition metal dichalcogenides. *npj Comput. Mater.* **7**, 31 (2021).
2. Zhou, J., Xu, H., Li, Y., Jaramillo, R. & Li, J. Opto-Mechanics Driven Fast Martensitic Transition in Two-Dimensional Materials. *Nano Lett.* **18**, 7794–7800 (2018).
3. Zhang, Y. & Fu, L. Terahertz detection based on nonlinear Hall effect without magnetic field. *PNAS* **118**, e2100736118 (2021).
4. Liu, L. *et al.* Phase-selective synthesis of 1*T′* $MoS_2$ monolayers and heterophase bilayers. *Nat. Mater.* **17**, 1108–1114 (2018).
5. Ghimire, S. *et al.* Observation of high-order harmonic generation in a bulk crystal. *Nat. Phys.* **7**, 138–141 (2011).
6. Ghimire, S. *et al.* Generation and propagation of high-order harmonics in crystals. *Phys. Rev. A* **85**, 043836 (2012).
7. Qian, X., Liu, J., Fu, L. & Li, J. Quantum spin Hall effect in two-dimensional transition metal dichalcogenides. *Science* **346**, 1344–1347 (2014).
8. Ma, E. et al. Recording interfacial currents on the subnanometer length and femtosecond time scale by terahertz emission. *Sci. Adv.* 5, 2 (2019).